Navier-Stokes Simulation of UH-60A Rotor/Wake Interaction Using Adaptive Mesh Refinement

Neal M. Chaderjian
Senior Research Scientist
Computational Aerosciences Branch
NASA Ames Research Center, Moffett Field, CA, 94035

ABSTRACT

Time-dependent Navier-Stokes simulations have been carried out for a flexible UH-60A rotor in forward flight, where the rotor wake interacts with the rotor blades. These flow conditions involved blade vortex interaction and dynamic stall, two common conditions that occur as modern helicopter designs strive to achieve greater flight speeds and payload capacity. These numerical simulations utilized high-order spatial accuracy and delayed detached eddy simulation. Emphasis was placed on understanding how improved rotor wake resolution affects the prediction of the normal force, pitching moment, and chord force of the rotor. Adaptive mesh refinement was used to highly resolve the turbulent rotor wake in a computationally efficient manner. Moreover, blade vortex interaction was found to trigger dynamic stall. Time-dependent flow visualization was utilized to provide an improved understanding of the numerical and physical mechanisms involved with three-dimensional dynamic stall.

Nomenclature

a	Fluid speed of sound
A	Rotor disk area, πR^2, or airfoil reference area
c	Local rotor blade or airfoil chord length
c_{tip}	Rotor blade tip chord length
C_l	Airfoil lift coefficient, $\frac{\text{Lift}}{\frac{1}{2}\rho V_\infty^2 A}$
C_d	Airfoil drag coefficient, $\frac{\text{Drag}}{\frac{1}{2}\rho V_\infty^2 A}$
C_m	Airfoil pitching moment coefficient, $\frac{\text{Moment}}{\frac{1}{2}\rho V_\infty^2 A c}$
C_M	Rotor pitching moment coefficient, $\frac{\text{Moment}}{\frac{1}{2}\rho (\Omega R)^2 A R}$
C_N	Rotor normal force coefficient, $\frac{\text{Normal Force}}{\frac{1}{2}\rho (\Omega R)^2 \text{A}}$
C_Q	Torque coefficient, $\frac{\text{Torque}}{\rho (\Omega R)^2 A R}$
C_T	Thrust coefficient, $\frac{\text{Thrust}}{\rho (\Omega R)^2 A}$
d	RANS turbulent length scale, distance from a field point to closest body surface
$\overline{d}$	DES length scale
FM	Figure of merit, $\frac{C_T^{3/2}}{\sqrt{2} C_Q}$
k	Reduced frequency of airfoil oscillation, $\frac{\omega c}{2 V_\infty}$
L_1	Level 1 Cartesian grid
M'	Sectional blade pitching moment
M_{tip}	Blade tip Mach number, $\frac{\Omega R}{a}$
M_∞	Freestream Mach number
$M^2 c_m$	Sectional pitching moment coefficient, $\frac{M'}{\frac{1}{2}\rho a^2 c^2}$
$M^2 c_n$	Sectional normal force coefficient, $\frac{N'}{\frac{1}{2}\rho a^2 c}$
N'	Sectional blade normal force
NB	Near body
OB	Off body
r	Radial position
R	Rotor radius
Re_{Tip}	Blade-Tip Reynolds number, $\frac{\rho V_{tip} c_{tip}}{\mu}$
V_∞	Freestream velocity
V_{tip}	Rotor tip velocity, ΩR
V_{LE}	Blade leading-edge velocity
x, y, z	Cartesian coordinates
y^+	Non-dimensional viscous wall spacing
α	airfoil angle of attack, deg
α_a	airfoil amplitude of oscillation, deg
α_m	airfoil mean angle of oscillation, deg
α_s	Rotor shaft angle, deg
β	Blade flap angle or sideslip angle, deg
ΔS	Off-body L_1 grid spacing
Δt	Time step, deg rotation
ζ	Blade lag angle, deg
θ	Blade pitch angle, deg
μ	Advance ratio, M_∞/M_{tip}, or fluid viscosity
ξ, η, ζ	Generalized curvilinear coordinates
ρ	Fluid density
σ	Geometric solidity
ψ	Azimuthal angle of rotor blade, deg
ω	airfoil angular frequency
Ω	Rotor rotational speed or vorticity magnitude

Introduction

Modern helicopter designs are utilizing novel aerodynamic concepts and propulsive technologies to meet the demanding requirements of civil aviation. One goal of

Presented at the AHS International 73rd Annual Forum & Technology Display, Fort Worth, TX, USA, May 9-11, 2017.

NASA's Revolutionary Vertical Lift Technology (RVLT) project is to develop high-fidelity computational fluid dynamic (CFD) tools with increased predictive accuracy to support the development of new commercial designs that can fly faster, with reduced noise, and lift heavier payloads in an environmentally responsible manner.

However, these new designs can encounter flight conditions where the rotor wake remains in close proximity to the rotor blades. When this happens, two common and challenging phenomena, blade vortex interaction (BVI) and dynamic stall, may occur. BVI is a condition where the blade-tip vortices pass in close proximity to a rotor blade, causing impulsive changes in pressure and high sound levels. Dynamic stall in level flight is a condition where the rotor reaches it thrust limit during heavy load conditions, causing a significant increase in blade torsion and control system loads, Bousman (Ref. 1). Dynamic stall also limits a helicopter's flight speed and produces significant structural vibration. Although dynamic stall may occur when there is no blade/wake interaction, BVI can affect both how and when dynamic stall occurs. This BVI/dynamic stall interaction will be discussed in this paper.

In 2011, Chaderjian and Buning (Ref. 2) showed that CFD hover performance and rotor blade airloads were not significantly affected by resolving the blade-tip vortices in the rotor wake (see Fig. 1) as previously thought. Rather, it was crucial to resolve the vortex formation at the blade tip through a combination of fine surface meshes and high-order spatial accuracy, and maintain a physically realistic turbulent eddy viscosity in the rotor wake, e.g., using a detached eddy simulation (DES) turbulent length scale. Since that time there has been a renewed interest in evaluating CFD prediction of hover performance using high-fidelity CFD methods, including an AIAA Rotorcraft Simulation working group (Ref. 3).

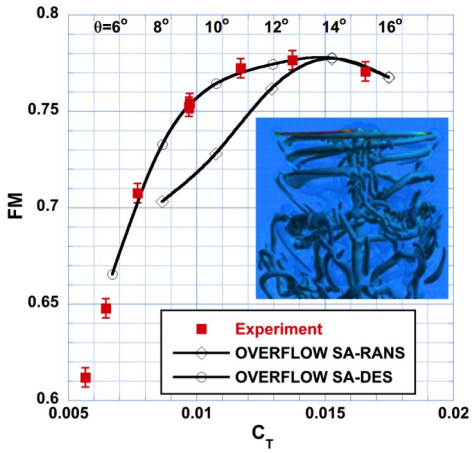

Figure 1. Figure of merit variation with C_T for the TRAM rotor in hover. Coarse wake grid spacing: ΔS=10% c_{tip}. M_{tip}=0.625, Re=2.1 million, Ref. 2.

Chaderjian and Ahmad (Refs. 4-5) later showed that the performance for a UH-60A rotor in level forward flight also did not depend significantly on resolving the tip vortices in the rotor wake. However, this example involved a rotor wake that descended downward and aft from the rotor blades (see Fig. 2). This result was not surprising because the vortex wake did not directly interact with the rotor blades.

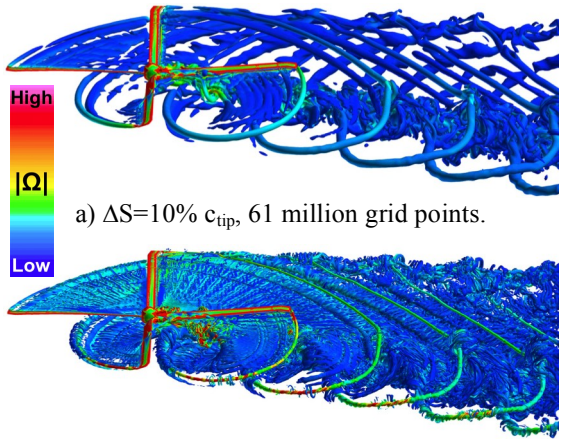

a) ΔS=10% c_{tip}, 61 million grid points.

b) ΔS=2.5% c_{tip}, 754 million grid points.

Figure 2. UH-60A rotor wakes colored by vorticity magnitude. Q-criterion iso-surface. Counter 8534. (Refs. 4-5)

An important question remains: How does the prediction of rotor airloads depend on tip-vortex resolution in the rotor wake, especially when the tip vortices remain in the rotor plane and are free to interact with the rotor blades? The occurrence of BVI and/or dynamic stall may further influence the effect the vortex wake has on the blade airloads. This is a practical consideration because it often requires an order-of-magnitude or more grid points to resolve rotor wakes with more realistic vortex-core sizes, compared to the engineering approach shown in Fig. 2a. An engineering approach typically uses a rotor wake grid spacing of ΔS=10% c_{tip}, the initial size of a blade vortex diameter during hover (Ref. 6), resulting in a greatly diffused numerical vortex. On the other hand, more realistic vortex core sizes are obtained when using a wake grid spacing of ΔS=2.5% c_{tip} (Ref. 5), (see Fig. 2b). But the computational cost can exceed the resources available for most engineering analysis.

The goal of this paper is to examine the affects of wake-grid resolution on the prediction of rotor blade airloads, when the vortex wake interacts with the rotor blades. Moreover, time-dependent numerical flow visualization is also used to better understand the mechanisms involved with two-dimensional (2D) and three-dimensional (3D) dynamic stall. Some of the similarities and differences will be discussed. The following sections include a description of the flight-test data, numerical approach, numerical results, and concluding remarks.

Flight-Test Data and Qualitative Analysis

NASA and the US Army, as a part of the UH-60A Airloads Program, maintain an extensive flight-test database (Ref. 7) for the Blackhawk helicopter in level trimmed flight and transient maneuvers (see Fig. 3). The UH-60A blade properties are listed in Table 1, while Table 2 lists three steady flight counters discussed in this paper.

Figure 3. Sikorsky UH-60A Blackhawk helicopter.

Table 1. UH-60A rotor properties.

Parameter	Value
Number of Blades	4
Radius, R	26.83 ft
Tip Chord, c_{tip}	20.76 in
Equivalent Blade Twist	-18 deg
Blade Tip Sweep	20 deg aft
Geometric Solidity, σ	0.0826
Airfoils	SC1095, SC1094R8
Thickness	9.5% chord
Nominal Rotor Speed	258 rpm
Nominal Tip Speed	725 ft/sec

Table 2. Flight counter flow conditions.

Flight Counter	M_∞	M_{Tip}	μ	Re_{Tip}	α_s, deg	β, deg	C_T
C8534 (High Speed)	0.236	0.642	0.368	6.86×10^6	-7.31	1.28	0.00651
C8513 (BVI)	0.0982	0.643	0.153	7.15×10^6	0.75	7.71	0.00657
C9017 (Dynamic Stall)	0.158	0.666	0.237	4.62×10^6	-0.15	-1.58	0.0110

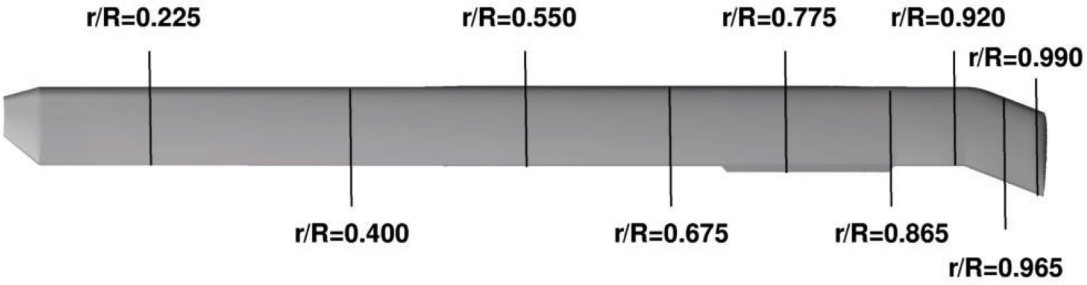

Figure 4. UH-60A flight-test measurement stations.

The UH-60A airloads database provides aerodynamic pressures, structural loads, and rotor forces and moments at 9 radial locations shown in Fig. 4. A static trim tab is deflected to ensure that each blade flies in a similar manner with minimal vibration. These deflections are unique to each Blackhawk helicopter, but the CFD simulations assume zero deflection.

Acquiring in-flight measurements on a moving and deforming rotor blade is very challenging, and this database does have some unresolved discrepancies. For example, the measured rotor thrust was determined from the helicopter's gross weight and estimates of the loads on the fuselage and tail rotor. Measured pitch and roll moments at the hub were determined from a bending moment gauge located on the upper rotor shaft, but the integration of the measured blade pressures sometimes compared poorly with the measured thrust and moments. For example, Potsdam et al. (Ref. 8) point out that the integrated thrust for flight counter C8534 was 10% higher than the measured thrust. Moreover, the integrated hub moment was 50% larger with an 80-deg phase difference compared to the measured pitching moment. Some of these discrepancies have been attributed to the discovery of bad pressure taps, with the greatest effect on the pitching moments. It is therefore common practice, and the one adopted here, to subtract out the mean forces and moments over a rotor revolution for validating CFD results with measurement.

Bousman (Ref. 1) carried out a qualitative analysis of three dynamic stall conditions, including level-flight counter C9017, which is examined in this paper and used for additional CFD validation. He identified where moment and lift stall occurred, and regions of flow separation on the rotor blades. He associated moment stall with the formation of a dynamic stall vortex at the blade leading edge, and lift stall occurring when the dynamic stall vortex passed over the trailing edge. He also identified when flow separation occurred at the blade trailing edge. He

considers these results qualitative (Ref. 1, 9) because he examined pressure time histories and made judgments of when these three events occurred.

Numerical Approach

The OVERFLOW Navier-Stokes CFD code and the CAMRAD II helicopter comprehensive analysis code are solved together in a loosely coupled manner to simulate trimmed level flight for a flexible UH-60A isolated rotor. These codes and the coupling process are described below.

CAMRAD II Code: CSD and Rotor Trim

The helicopter comprehensive analysis code, CAMRAD II (Ref. 10), provides computational structural dynamics (CSD) and rotor trim control angles for a coupled CFD/CSD simulation. This code is widely used in the helicopter industry and models a flexible rotor blade using nonlinear finite elements. CAMRAD II has its own simplified low-fidelity aerodynamic model.

Fluid/Structure Interaction: Loose Coupling

For static flight conditions, like those described in Table 2, a loose-coupling procedure between CFD and CSD is used every ¼ revolution following the approach of (Ref. 8), where OVERFLOW CFD airloads are transferred to CAMRAD II and CAMRAD II blade deflections and trim angles are transferred to OVERFLOW.

The coupling procedure is valid as long as the rotor loads are periodic. This does not preclude some aperiodicity in the vortex wake, which is often the case in a high-resolution turbulent flow simulation. If the rotor loads are not periodic, e.g., a maneuvering vehicle, then a loose-coupling procedure is not time accurate. In this case, a tight-coupling procedure is required, where data is exchanged between OVERFLOW and CAMRAD II every time step.

The process for running the coupled OVERFLOW and CAMRAD II codes is accomplished using a C-shell script. This script helps automate the run process, which uses several CAMRAD II tools and coupling steps. Additional details can be found in (Ref. 4).

OVERFLOW 2.2 CFD Code

OVERFLOW is a finite-difference, overset grid, Navier-Stokes flow solver. The time-dependent, Reynolds-averaged, Navier-Stokes (RANS) equations are solved in strong conservation-law form

$$\frac{\partial Q}{\partial t} + \frac{\partial (F - F_v)}{\partial x} + \frac{\partial (G - G_v)}{\partial y} + \frac{\partial (H - H_v)}{\partial z} = 0 \qquad (1)$$

where $Q=[\rho,\ \rho u,\ \rho v,\ \rho w,\ e]^T$ is the vector of conserved variables; F, G, and H are the inviscid flux vectors; and F_v, G_v, and H_v are the viscous flux vectors. A duel time-stepping, implicit approximate factorization scheme in delta form is used to solve Eq. (1) in generalized coordinates by

$$\left[I + h\partial_\xi \hat{A}^k\right]\left[I + h\partial_\eta \hat{B}^k\right]\left[I + h\partial_\zeta \hat{C}^k\right]\Delta\hat{Q}^k = -hR^{k,n} \qquad (2)$$

where

$$R^{k,n} = \frac{3\hat{Q}^k - 4\hat{Q}^n + \hat{Q}^{n-1}}{2\Delta t} + \left(\hat{F} - \hat{F}_v\right)_\xi^k + \left(\hat{G} - \hat{G}_v\right)_\eta^k + \left(\hat{H} - \hat{H}_v\right)_\zeta^k$$

and

$$h = \frac{2\Delta t \Delta \tau}{2\Delta t + 3\Delta \tau}$$

In these equations, $\hat{Q} = Q/J$, where J is the transformation Jacobian, and $\hat{A}$, $\hat{B}$, and $\hat{C}$ are the transformed flux Jacobian matrices. The superscript *k* is the subiteration index, while the superscript *n* is the time-step index. The physical and pseudo (relaxation) time steps are Δt and $\Delta\tau$, respectively. Finally, $\Delta\hat{Q}^k = \hat{Q}^{k+1} - \hat{Q}^k$, where subiteration convergence implies that $\hat{Q}^k \to \hat{Q}^{n+1}$, which is 2nd-order accurate in time.

Equation 2 is solved using the Pulliam-Chaussee diagonal algorithm (Ref. 11), and the spatial derivatives are evaluated with 5th-order central differencing. The 5th-order central differencing is a combination of a 6th-order central operator and a 5th-order artificial dissipation term. Further details of OVERFLOW's spatial accuracy are described in (Ref. 12), while the many options available within the code are described in (Refs. 13-14).

A time step of Δt=¼° blade rotation with 60 subiterations is used throughout this paper. This nominally exceeds a 2.3-order subiteration residual drop between time steps for all grids and cases, which has been shown to provide converged time-accurate forces and moments on the rotor (Ref. 4).

Overset Grids

OVERFLOW solves the Navier-Stokes equations in an inertial coordinate system, where overset body-conforming O-grids rotate through a fixed Cartesian background grid system. Figure 5 shows the near-body (NB) grids that are used to resolve the flow in the vicinity of the rotor blades. Each rotor blade consists of 4 grids: one inboard cap grid, two main body grids, and one outboard cap grid. The two cap grids resolve the inboard blade tip (blade root) and the outboard blade tip. The main blade O-grid is split into upper and lower grids to facilitate future NB adaptive mesh refinement (AMR) applications. Three NB grids are also used to resolve the flow on a simplified rotor hub (see Fig. 5c). The hub rotates with the rotor blades, however, the linkage between the hub and the blades is neglected.

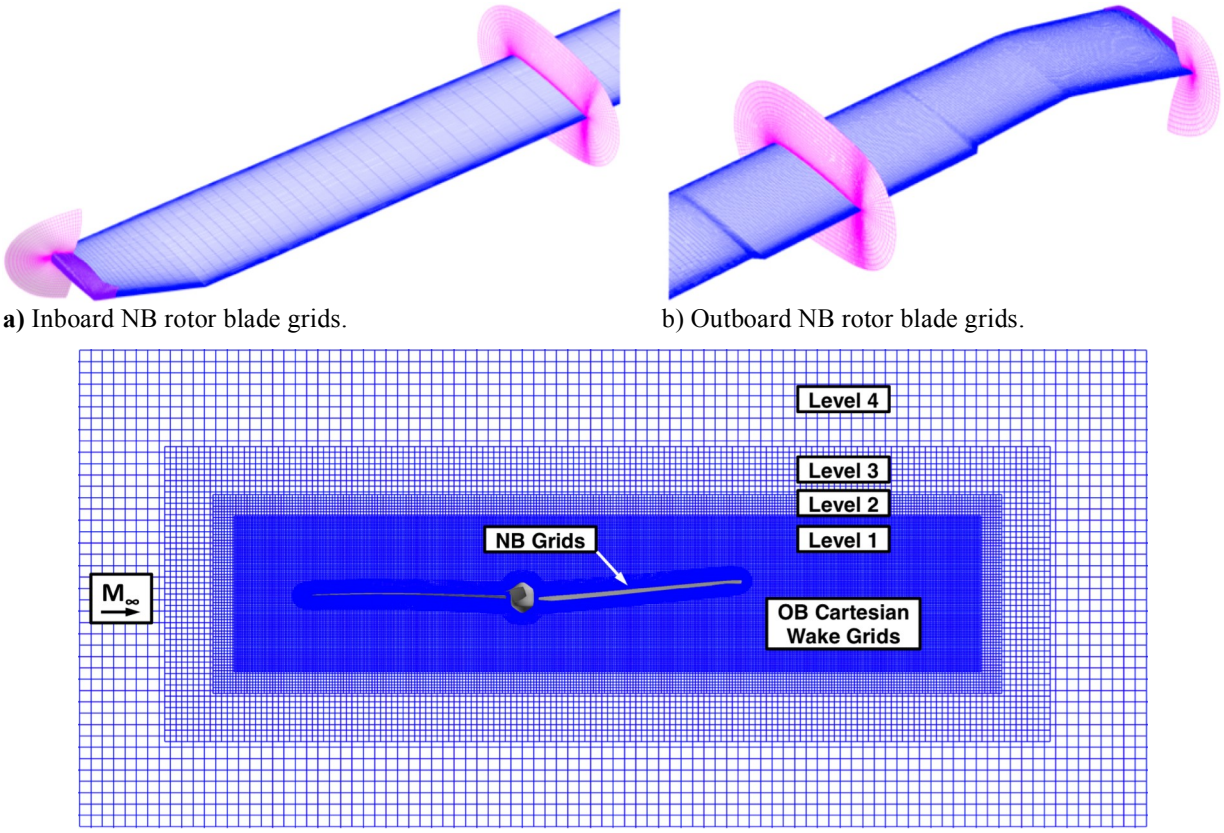

a) Inboard NB rotor blade grids.

b) Outboard NB rotor blade grids.

c) Cartesian OB grid system.

Figure 5. UH-60A rotor-blade overset grid system.

Surface grid resolution on the rotor blades is clustered in the chordwise direction near the airfoil leading and trailing edges to accurately resolve large pressure gradients. The spanwise resolution along the rotor blade is nearly uniform, to better resolve the dynamic stall vortex, and clustered near the blade tip to accurately resolve the formation of the blade-tip vortex. The normal grid spacing at the blade surface maintains a $y^+<1$. All curvilinear body grids have a stretching ratio of less than 10% in all three coordinate directions. This helps reduce the algorithm's spatial truncation error.

An off-body (OB) Cartesian grid system, shown in Fig. 5c, is designed to resolve the off-body vortex wake and extend the computational domain to the far field. Uniform Cartesian grids have constant transformation metrics with a 0% stretching ratio. Solutions are obtained by using a uniform OB Cartesian grid spacing of ΔS=10%, 5% or 2.5%c_{tip}. This Level-1 Cartesian grid typically forms a box surrounding the entire rotor system and a portion of the vortex wake of interest. Additional "brick grids" are automatically added to the Level-1 grid to rapidly extend the computational domain to the far field, which for the present computations is about 5 rotor radii from the blades in all three directions. These brick grids are referred to as Levels 2, 3, 4, etc., each of which is a factor of 2 coarser in all three coordinate directions than the previous grid level.

Table 3 summarizes grid size statistics for all flow solutions presented in this paper. The NB grids are always the same. However, the OB Cartesian grids may vary in number and size depending on the vortex wake physics and OB grid resolution.

Table 3. Summary of UH-60A overset grid size.

Grid Type	Number of Grids	Surface Grid Points	Volume Grid Points
Rotor Blade	4	117,763	11.8 million
Rotor Hub	3	28,875	2.5 million
Total (Near and Off-Body)	750-14,700	499,927	83 million – 1.8 billion

Dynamic Adaptive Mesh Refinement

A dynamic NB (Ref. 15) and OB (Ref. 16) AMR capability has been implemented within OVERFLOW. However only OB AMR is used in the present simulations. Cartesian grids are automatically added in the rotor wake region to improve or maintain the resolution of the turbulent wake and blade-tip vortices. The results in this paper use a vorticity magnitude sensor function to find and refine the vortex wake, see (Ref. 5) for additional details.

OB AMR grids begin with Cartesian Level-1 grid resolution, ΔS, and depending on user input, may refine the rotor wake to a much finer level through successive overlapping grids. Each level of refinement decreases the local Cartesian grid spacing by a factor of two in each coordinate direction. Thus a two-level OB AMR refinement would identify the vortical structures and overlay the surrounding Level-1 Cartesian grid spacing (ΔS) with two more Cartesian grids with grid spacing ½ ΔS and ¼ ΔS. The local grid size grows by 8X for each level of refinement. This approach is more efficient than selecting a single larger Cartesian region of grid spacing ¼ ΔS to resolve the entire rotor wake. Overlapping grids of different resolution transfer data between grids with tri-linear interpolation.

A somewhat different OB AMR strategy is employed in this paper that eliminates interpolation errors within the resolved rotor wake. This is accomplished by only using Level-1 grids throughout the resolved rotor wake region (see Fig. 7).

The procedure begins by surrounding all NB rotor grids with a Level-1 Cartesian grid. OB AMR is then used to extend the Level-1 region and capture the rest of the rotor wake with additional Level-1 Cartesian grids. Level-1 grids share the same grid spacing, ΔS, and therefore have coincident grid points when they overlap with each other. Data is therefore transferred between these Level-1 wake grids by direct injection, i.e., no interpolation is required. Tri-linear interpolation is only needed near the boundaries of NB grids and brick grids.

The outer-boundary grid spacing for NB grids is specified to be $5\%c_{tip}$. So three OB AMR grid resolutions, namely ΔS = 10%, 5%, and 2.5% c_{tip}, can be used while maintaining a factor of two resolution between the wake grids and the NB or brick grids.

Further details on the use of OVERFLOW's OB AMR to rotor applications can be found in Chaderjian (Ref. 5).

Turbulence Model

The OVERFLOW code has a choice of algebraic, one-equation and two-equation turbulence models (Ref. 13), including hybrid RANS/LES (large eddy simulation) models that close the Reynolds-averaged equations. The UH-60A rotor simulations presented in this study use the one-equation Spalart-Allmaras (SA) turbulence model (Ref. 17) primarily within the boundary layer. Outside the boundary layer, the SA turbulence model functions as a sub-grid scale (SGS) model in a detached eddy simulation (DES) sense (Ref. 18) when the Reynolds stresses are grid resolved. The DES length scale is crucial in limiting the turbulent eddy viscosity to more physically realistic values in a rational (non ad hoc) manner. This insures that fully turbulent hover airloads and turbulent rotor wakes can be more realistically modeled and resolved (Refs. 2, 4, and 5).

The DES length scale is defined in terms of the original RANS length scale and local grid spacing by

$$\bar{d} = \min\left(d, C_{DES}\Delta\right) \tag{3}$$

where Δ=max(Δx, Δy, Δz), and C_{DES}=0.65. The SA rotation and/or streamline curvature (SARC) correction due to Shur et al. (Ref. 19) is also included. Moreover, the shielding function introduced by Spalart et al. (Ref. 20), also referred to as delayed detached eddy simulation (DDES), is used to ensure that the SA-RANS model remains fully active within the turbulent boundary layer. This prevents the DES length scale from inadvertently activating within the boundary layer. This can happen when the local grid spacing is very fine, causing a modeled stress depletion that leads to grid-induced flow separation and non-physical results. Further details of the SA-DES hybrid turbulence model used in the current rotor simulations are described in (Refs. 2, 4, and 5).

The OVERFLOW CFD code is also used to simulate 2D dynamic stall, which provides a basis to compare and contrast 2D and 3D dynamic stall phenomena. The SA-RANS turbulence model is used in this special case, because a LES approach requires a third dimension to allow for the nonlinear energy cascade from larger turbulent scales to smaller ones. A SA-DES approach is therefore inappropriate for 2D flows.

Numerical Results

The OVERFLOW Navier-Stokes CFD code is used throughout this study to simulate the flow for an isolated UH-60A rotor in forward flight, and a 2D airfoil oscillating in pitch. Figure 6 also highlights some key flow conditions and parameters used in the discussion of the UH-60A rotor in forward flight.

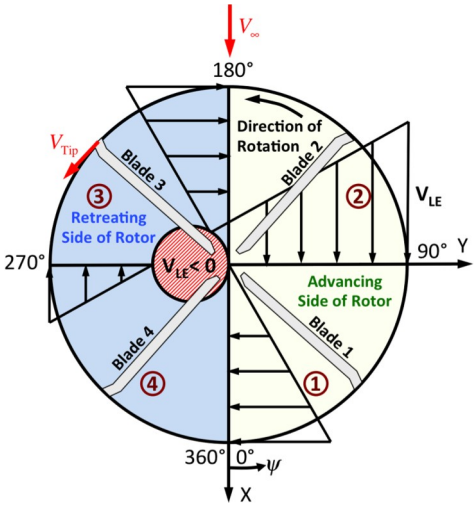

Figure 6. Flow conditions for forward flight.

All CFD computations were carried out at the NASA Advanced Supercomputing (NAS) facility on the Pleiades supercomputer, which currently has 246,049 CPU cores consisting of Intel Broadwell, Haswell, Ivy Bridge, and

Sandy Bridge nodes. The current UH-60A CFD simulations use 5,628 Broadwell cores that run at 2.4 GHz. Each Broadwell node consists of 28 cores and 128 GB of memory. Data is saved to a 29PB Lustre filesystem for post-processing and the creation of time-dependent flow visualization. The 2D airfoil simulation only used 1 Broadwell node (28 cores).

Blade Vortex Interaction: UH-60A (C8513)

The first flow condition is flight counter C8513, where the rotor wake initially remains in the plane of the rotor blades, giving rise to a BVI condition. Figure 7 shows the capture of the vortex wake with L_1 Cartesian grids on a longitudinal cutting plane. Three OB AMR grid resolutions were used, ΔS=10% c_{tip}, ΔS=5% c_{tip}, and ΔS=2.5% c_{tip}. The AMR process produces a fairly steady number of grids and grid points, once the solution process reaches dynamic equilibrium. A representative number of grid points for each OB AMR resolution is listed in Fig. 7. Gray-scale vorticity contours highlight the vortex wake, and the finer grids appear darker.

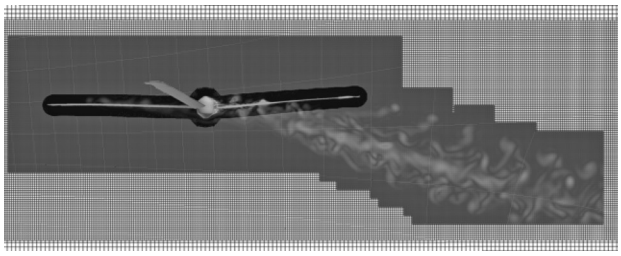

a)ΔS=10% c_{tip}, 87 million grid points.

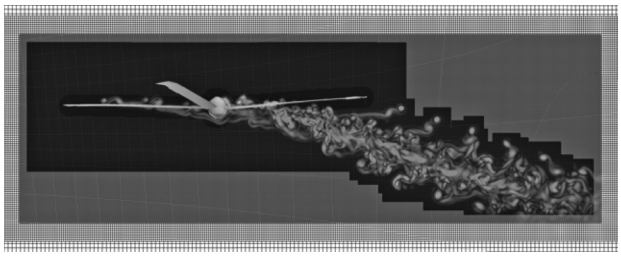

b)ΔS=5% c_{tip}, 297 million grid points.

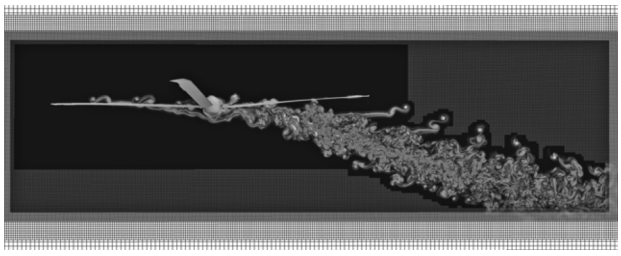

c)ΔS=2.5% c_{tip}, 1.8 billion grid points.

Figure 7. Side view of vortex wakes and OB L_1 AMR grids (vorticity magnitude gray scale). Counter 8513.

Figure 7 shows a generous L_1 Cartesian grid (dark rectangle) that surrounds the rotor blades and hub system. BVI occurs mostly on the upwind side (front half) of the rotor disk where the rotor wake remains close to or slightly above the rotor blades. However, the wake descends downward aft of the rotor hub. The OB AMR is active up to 2.5R downwind from the hub center. The grids are allowed to further coarsen downwind of the AMR region. The far-field boundaries extend approximately 5R in all directions, sufficient for forward flight conditions (Ref. 4).

More turbulent flow features and stronger vortices (light gray shading) are better resolved with the finer OB meshes. The AMR tightly surrounds the vortical flow, especially at the highest resolution. The same set of AMR parameters were used for hover and forward flight (Refs. 2, 4, and 5), and do not need adjustment for this class of flows. The AMR adapts to the vorticity magnitude every degree of rotation.

Figure 8 is an overhead view (cutting plane below the rotor blades) of the L_1 AMR grid system for ΔS=2.5% c_{tip}. The dark rectangle is the specified L_1 grid. The AMR grids tightly capture the rolled-up tip vortices on both sides of the rotor, and individual blade-tip vortices in the lower wake. The wake system is slightly skewed to one side due to the sideslip condition (see Table 2).

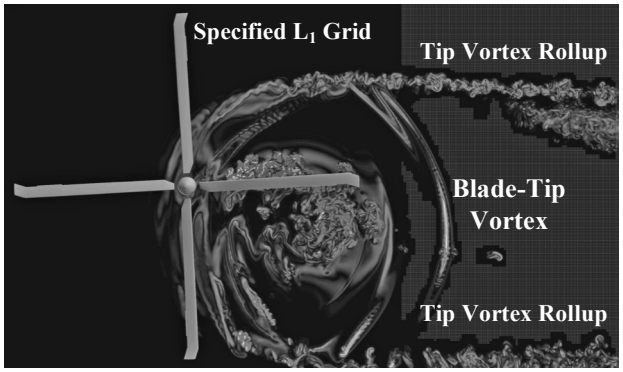

Figure 8. Top view of vortex wake and OB L_1 AMR grids (vorticity magnitude gray scale). ΔS=2.5% c_{tip}, 1.8 billion grid points.

Figure 9 shows an oblique view of the rotor's tip vortices and wake for all three OB AMR resolutions using iso-surfaces of the q-criterion. The blade-tip vortices coalesce into a larger vortex on both sides of the rotor, near ψ=90° and 270°, and there is flow separation behind the rotor hub that interacts with the inboard portion of the rotor blade when $\psi = 0^\circ$. BVI occurs when the blade-tip vortices pass very close to the upper surface of the rotor blades at 45° < ψ < 270°.

Figures 8-9 show that the blade-tip vortices have more realistic core sizes as the OB mesh is refined, but at a significant computational cost. For the present forward-flight case, converged OB resolutions of ΔS=10%, 5%, and 2.5% c_{tip} have total grid sizes of 87 million, 297 million, and 1.8 billion grid points, respectively.

The loose coupling convergence history for the blade-root control angles is shown in Fig. 10. The collective pitch angle, $\theta_\circ$, and the first harmonics, θ_{1c} and θ_{1s}, are all well converged within 5 rotor revolutions from an impulsive start. The convergence histories for all three OB resolutions are virtually identical. A similar convergence history is shown for the flapping, β, and lag angles, ζ.

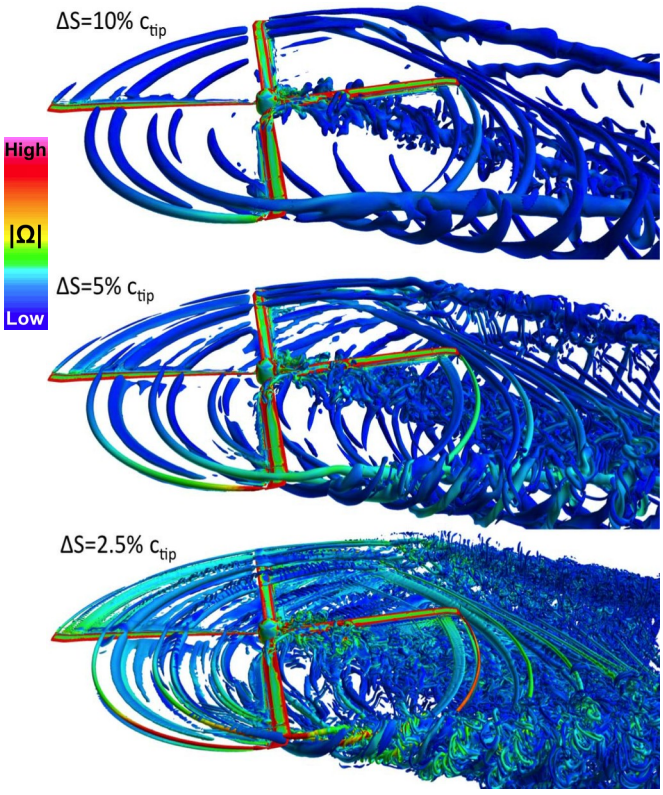

Figure 9. Oblique view of vortex wake colored by vorticity magnitude. Q-criterion iso-surface.

Figure 11 compares the computed mean normal force coefficient, C_n, mean pitching moment coefficient, C_m, and mean chord force coefficient, C_c, with the flight-test measurements. The sectional quantities are scaled by the square of the sectional Mach number, and the time dependency is removed by averaging over a complete rotor revolution. These quantities provide an overall average measure of prediction accuracy as a function of radial distance, r, along the rotor blade. The normal and chord force coefficients compare very well with the measurements. The computed pitching moments do a reasonable job of following the measured values, but there seems to be a surprising amount of scatter in the experiment. Note that the mean computed loads for all three OB AMR resolutions are virtually identical with each other.

The azimuthal variation of the computed normal force coefficient (minus the mean) is compared with experiment in Fig. 12 at four radial locations and for all three OB AMR resolutions. There is considerable variation of the normal force with azimuth angle at each radial location. The outboard peaks located near ψ=90° and 270° are the result of BVI (see also Fig. 9). Overall, the comparison is quite good for all three OB wake-grid resolutions. There is a slight phase difference between the coarsest OB grid resolution and the two finer ones, especially near the BVI azimuth locations. However, these differences are small from an airloads performance perspective.

The computed pitching moment coefficient (mean removed) is compared with experiment in Fig. 13. The comparison is quite good, similar to the results in Fig. 12. Once again there is a slight phase difference between the coarsest OB resolution and the two finer ones. Especially near the two outboard BVI events at ψ=90° and 270°. The BVI moment peak near ψ=270° is somewhat under predicted at r/R=0.865, but reasonably resolved at r/R=0.965, where the surface mesh is finer. NB AMR near the blade surface may improve the prediction of the pitching moment amplitude for the outboard radial locations.

Figure 14 compares the computed chord force coefficient (mean removed) with experiment at the same four radial locations. The chord force is more strongly influenced by viscous effects and therefore more challenging to predict than the normal force. Moreover, accurately measuring the chord force has some practical considerations, such as a limited number of pressure taps. Nevertheless, the computed values compare well with the measured values, especially at the two outboard radial stations. There are some small differences between the coarsest and two finer OB resolutions, as in the normal force and pitching moments. However, there is a more significant discrepancy between computation and experiment at the inboard most station, r/R=0.400, near ψ=360°. This is where the blade root is directly downwind and immersed in the separated wake of the hub.

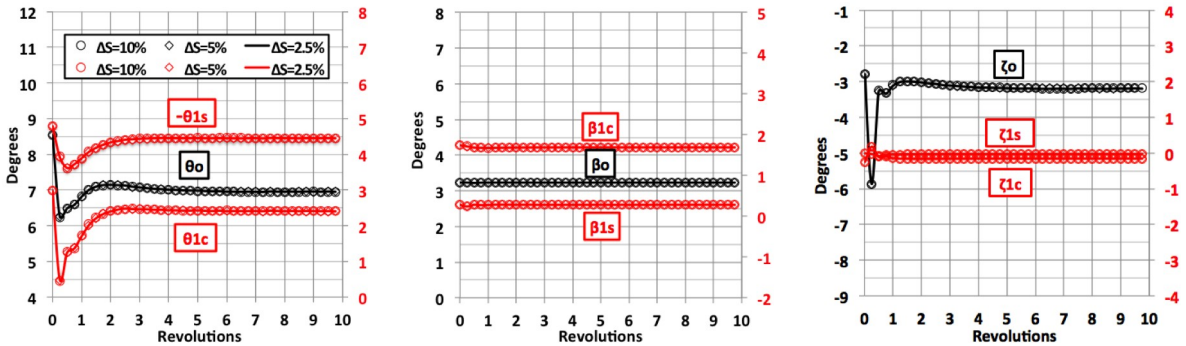

Figure 10. Loose coupling blade-root control angle convergence history.

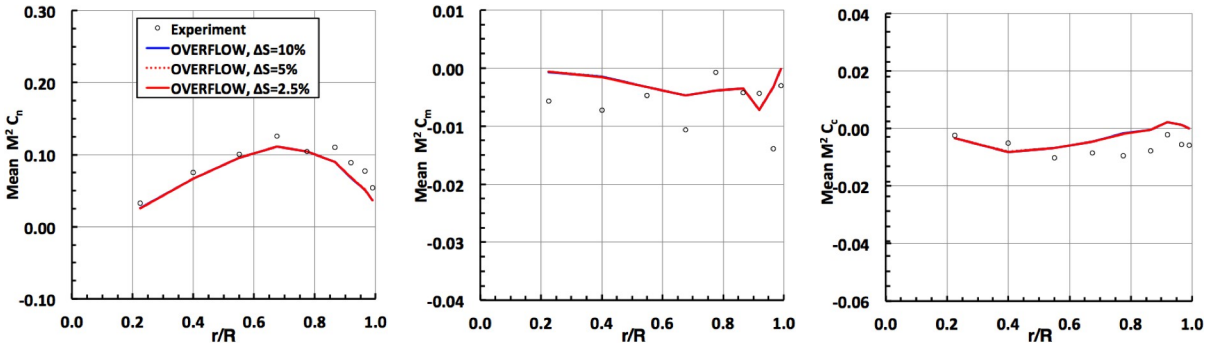

Figure 11. Comparison of mean sectional airloads (azimuthally averaged).

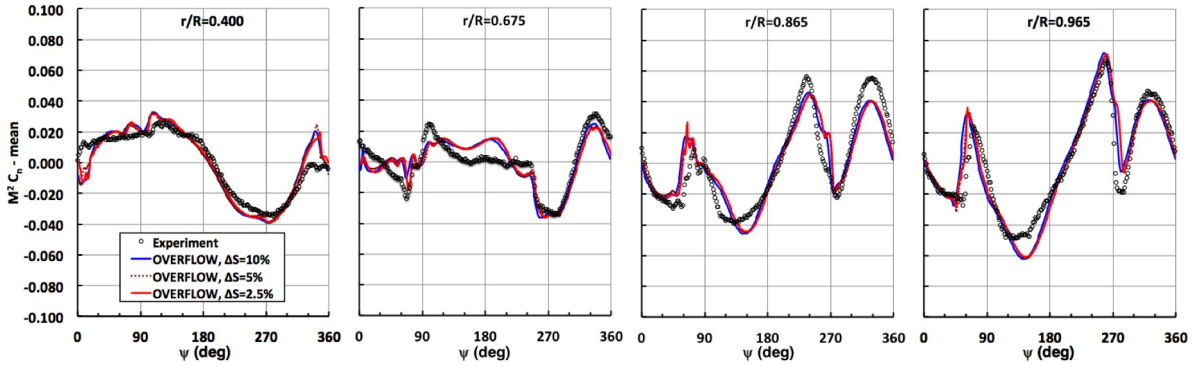

Figure 12. Comparison of normal force coefficient (mean removed) at four radial stations.

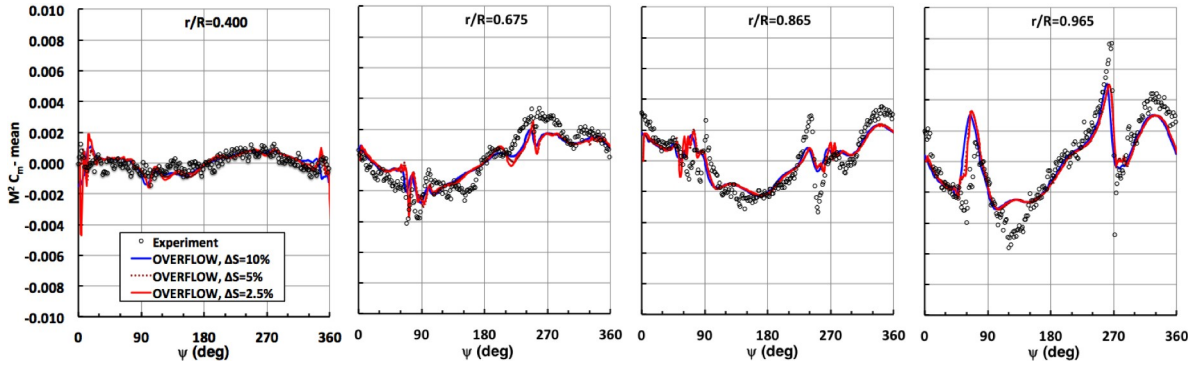

Figure 13. Comparison of pitching moment coefficient (mean removed) at four radial stations.

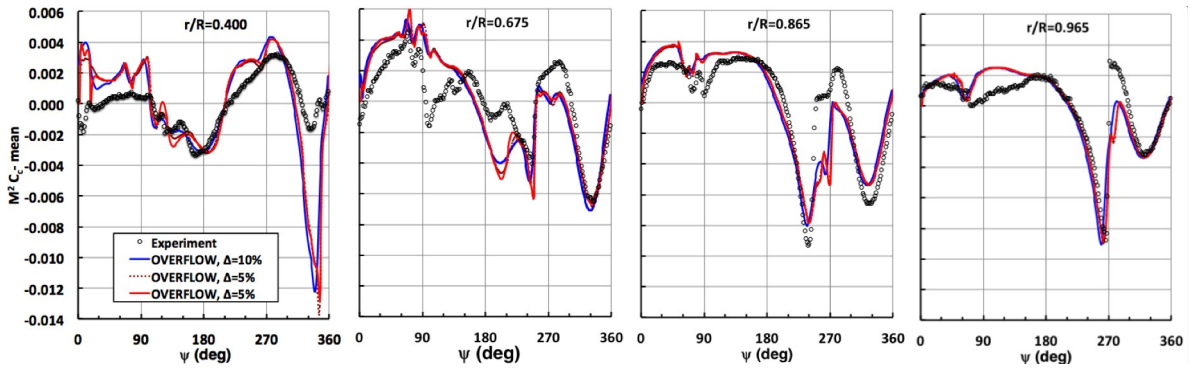

Figure 14. Comparison of chord force coefficient (mean removed) at four radial stations.

Figure 15 shows an image based flow visualization (IBFV) (Ref. 21) of the time-dependent CFD flow patterns on the upper rotor blade surface (colored by pressure) for ψ=0°, 90°, 180°, and 270°. The surface-flow patterns appear very two dimensional, especially along the outboard half of the rotor blades. This is typical of rotor blades that are predominantly unswept wings, except near the blade tip. The inboard surface flow indicates significant three dimensionality and flow separation for ψ=0°, and 270°. The inboard part of the blade at ψ=0° lies directly in the separated wake of the rotor hub. For ψ=270°, the inboard part of the blade has reversed flow, as indicated by Fig. 6. The advancing rotor blade, ψ=90°, appears two-dimensional with attached flow throughout its entire span, consistent with Fig. 6.

Overall, the three OB wake-grid resolutions were not found to significantly affect the predicted performance of the rotor. The coarser grid resolution, $\Delta S=10\%c_{tip}$, seems sufficient for engineering analysis. Very slight differences between the coarsest and finer resolutions where eliminated once the OB wake-grid resolution was $\Delta S=5\%c_{tip}$ or finer, which may affect the acoustics. These results presume adequate resolution of the tip vortex formation through a combination of high-order spatial accuracy and surface-grid resolution, and the use of a DDES approach to control the growth of the turbulent wake eddy viscosity to more physically realistic values.

Table 4 summarizes the computer wall-clock time used for the three OB AMR resolutions. The computer time and cost grows significantly with OB grid resolution (see 4th column). However, the computational efficiency significantly improves with the larger grid sizes (see 6th column). The precise number of grids and grid points vary to a small degree as the solution evolves in time. The values shown in Table 4 are representative of converged values.

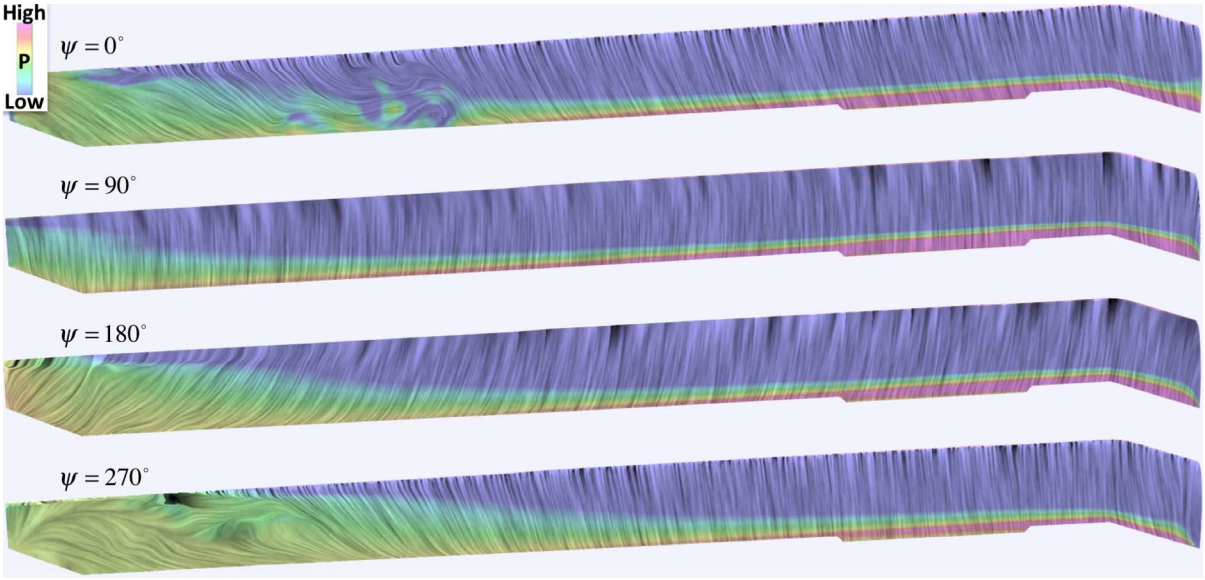

Figure 15. Top view of surface flow colored by pressure. $\Delta S=2.5\%\ c_{tip}$.

Table 4. Summary of computer wall-clock time using 5,628 Broadwell CPU cores with two threads.

BVI Counter C8513					
OB AMR Resolution	# Grids	# Grid Points	Time/Rev	Relative Time	Time/Rev/ 100 Million GP
$\Delta S=10\%c_{tip}$	500	87 million	4.6 hr	1.0	5.3
$\Delta S=5\%c_{tip}$	2,500	297 million	7.8 hr	1.7	2.6
$\Delta S=2.5\%c_{tip}$	12,000	1.80 billion	39.9 hr	8.7	2.2

Two-Dimensional Dynamic Stall

Dynamic stall is a challenging flow regime to accurately predict with CFD. This flow condition involves 3D flow separation that is strongly dependent on the blade motion relative to the freestream, the local angle of attack, and turbulence model. Rotor blade flexibility also contributes to the quantitative nature of the aerodynamic response.

Although dynamic stall for a helicopter rotor involves rapidly moving 3D flow separation, many in the research community believe its fundamental nature can be characterized with a simpler 2D airfoil oscillating in angle of attack, see Tan and Carr (Ref. 22). Some of the earliest experimental research by McCroskey et al. (Ref. 23) identified these 2D characteristics, namely a sudden drop in the normal force and pitching moment with pitch angle. More recent experiments include those by Chandrasekhara

and Ahmed (Ref. 24) and Ramasamy et al. (Ref. 25). This perspective will be shown to be somewhat over simplistic, especially when dynamic stall is accompanied by BVI.

An OVERFLOW simulation of a NACA 0015 airfoil undergoing a large-amplitude oscillation in angle of attack illustrates the nature of 2D dynamic stall. This simulation provides a basis to compare and contrast 2D and 3D dynamic stall phenomena.

The angle of attack for the pitching airfoil is defined as

$$\alpha = \alpha_m + \alpha_a \sin(2kt - \tfrac{\pi}{2}) \qquad (4)$$

where $\alpha_m = 10^\circ$, $\alpha_a = 10^\circ$, and k=0.1. The freestream Mach number M_∞=0.3 and Re=2.1 million based on the airfoil chord. There were 2,880 time steps per pitch cycle.

Figure 16 shows snapshots from a time-dependent visualization of the pitching NACA 0015 airfoil, and its aerodynamic response. The formation of the leading edge vortex during the upstroke (α=18°-19°) is associated with moment stall, while the traversal of the leading edge vortex past the airfoil trailing edge, α=20°, is associated with lift stall. The rollup of the boundary layers near the leading and trailing edges also indicate flow separation. For this flow, three distinct peaks can be observed for the lift and pitching moment response, and three drag-rise peaks are also noted. There are some phase differences between the three aerodynamic coefficients. According to Bousman (Ref. 1), two or three stall events per cycle are common and depend on the airfoil geometry and flow conditions. Each of the three stall events in this flow is associated with the formation and traversal of a different leading edge vortex.

Note that as the first vortex passes the trailing edge, at α=20°, it induces a strong secondary vortex (with opposite spin) at the trailing edge, causing reversed flow over the airfoil surface. As each successive leading edge vortex forms, it will be smaller and weaker than the previous one.

These 2D dynamic stall characteristics will be observed in the next section, which describes 3D dynamic stall for the UH-60A rotor in forward flight. However, some important differences will be identified.

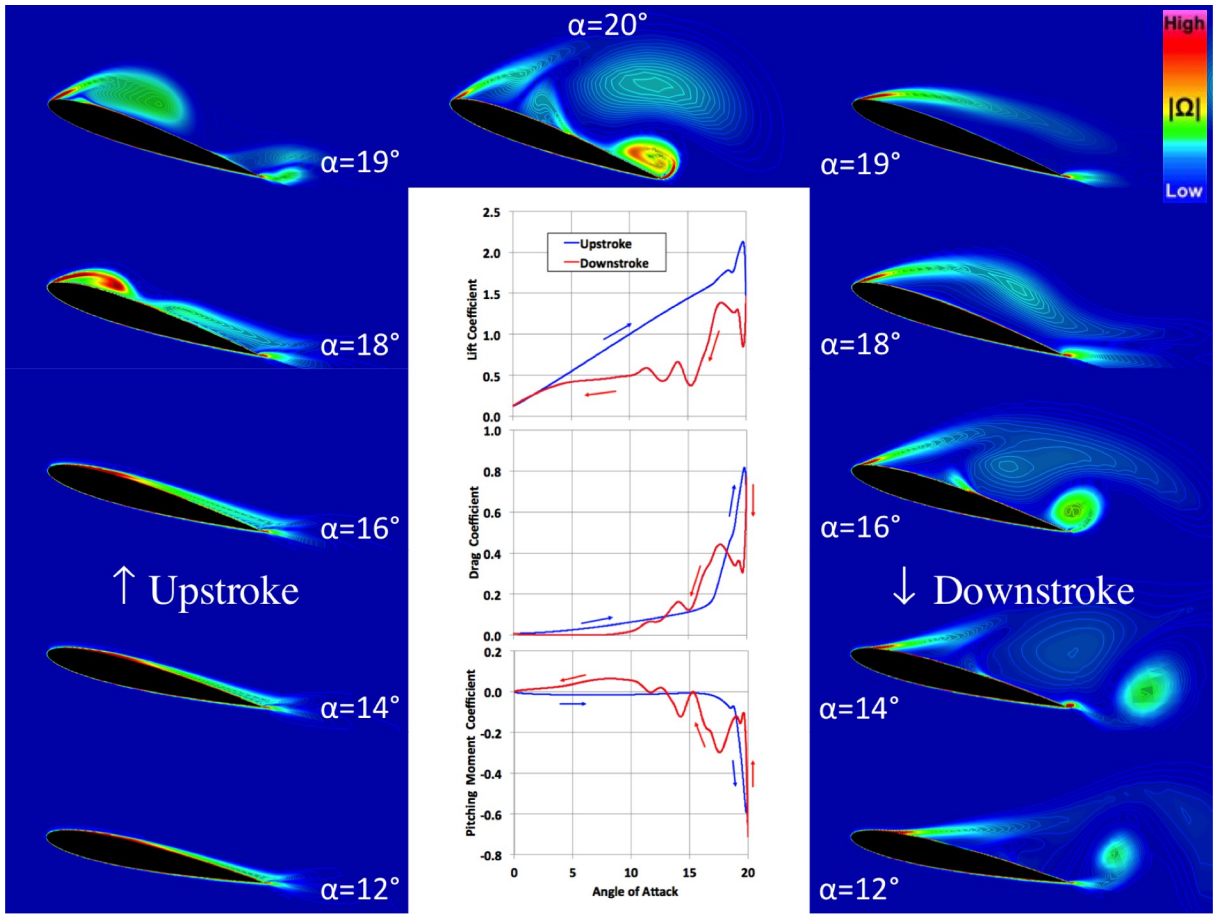

Figure 16. Time-dependent flow visualization (colored by vorticity magnitude) and aerodynamic response for a NACA 0015 airfoil undergoing dynamic stall.

Three-Dimensional Dynamic Stall: UH-60A (C9017)

Flight counter C9017 has a much higher thrust coefficient than the previous BVI case (see Table 2) leading to 3D dynamic stall. The vortex wake also interacts directly with the rotor blades, leading to a BVI condition that influences the dynamic stall. The flow physics is significantly more complex than flight counter C8513, and the 2D example in Fig. 16.

Figure 17 shows the capture of the vortex wake on a longitudinal cutting plane for three OB AMR grid resolutions, ΔS=10% c_{tip}, ΔS=5% c_{tip}, and ΔS=2.5% c_{tip}.

The L_1 box grid (gray rectangle) surrounds the rotor blades and hub system. The vertical extent of the L_1 box grid has been reduced compared to the previous BVI case in an effort to reduce the total grid size and computational cost. The AMR process is relied upon to a greater extent to capture the vortex wake. The three grid resolutions have total grid sizes of 83 million, 241 million, and 1.3 billion grid points, respectively. This represents a relative savings of 5%, 19%, and 28% compared to the previous BVI case. Moreover, the dynamic stall environment has more complex turbulent flow structures to resolve.

The finest meshes are once again more compact around the turbulent vortex wake (compare Fig. 17a and 17c). The descent of the vortex wake is shallow downwind of the rotor blades, creating strong blade/wake interaction. The far-field boundaries are the same as the previous BVI case.

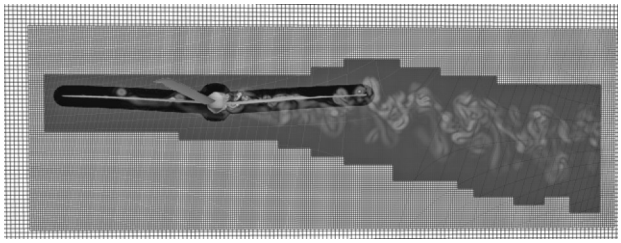

a)ΔS=10% c_{tip}, 83 million grid points.

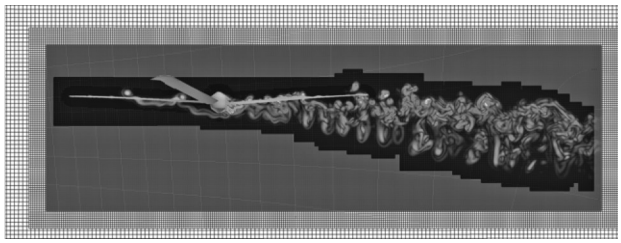

b)ΔS=5% c_{tip}, 241 million grid points.

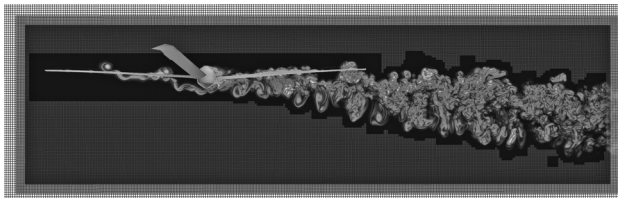

c)ΔS=2.5% c_{tip}, 1.3 billion grid points.

Figure 17. Side view of vortex wakes and OB L_1 AMR grids (vorticity magnitude gray scale). Counter 9017.

Figure 18 is an overhead view (cutting plane below the rotor blades) for the ΔS=2.5% c_{tip} AMR grid system. The dark rectangle is the specified L_1 box grid. The AMR grids once again tightly capture the vortical structures in the lower wake. Individual blade-tip vortices and the tip-vortex rollup on both sides of the rotor are identified in the figure. Note also that the 4th quadrant contains turbulent structures that advect downwind from a dynamic stall event. Using AMR to capture and resolve only the feature-rich regions can reduce the grid size and computational cost.

Figure 19 shows an oblique view of the rotor's tip vortices and wake for all three OB AMR resolutions. There is a significant progression of turbulent flow details as the OB grid is refined. The coarsest OB mesh has tip vortices that are greatly diffused and much larger in diameter than the finest mesh vortices. The coarse-mesh vortices are significantly weaker (green/blue color) and break up more readily than the fine-mesh vortices (red/yellow color). The wake shear-layers leaving blade trailing edges are better resolved on the finest mesh, and non-existent on the coarsest mesh. The finest AMR grids also show greater detail of the entrainment of the wake shear-layers and turbulent eddies into the blade-tip vortices.

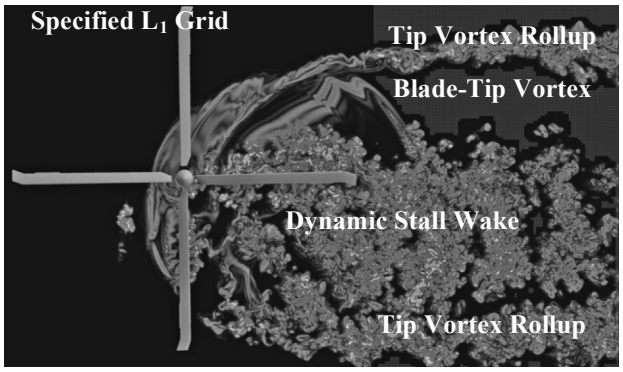

Figure 18. Top view (cutting plane below the rotor blades) of the vortex wake and off-body L_1 AMR grids (vorticity magnitude gray scale). ΔS=2.5% c_{tip}, 1.3 billion grid points.

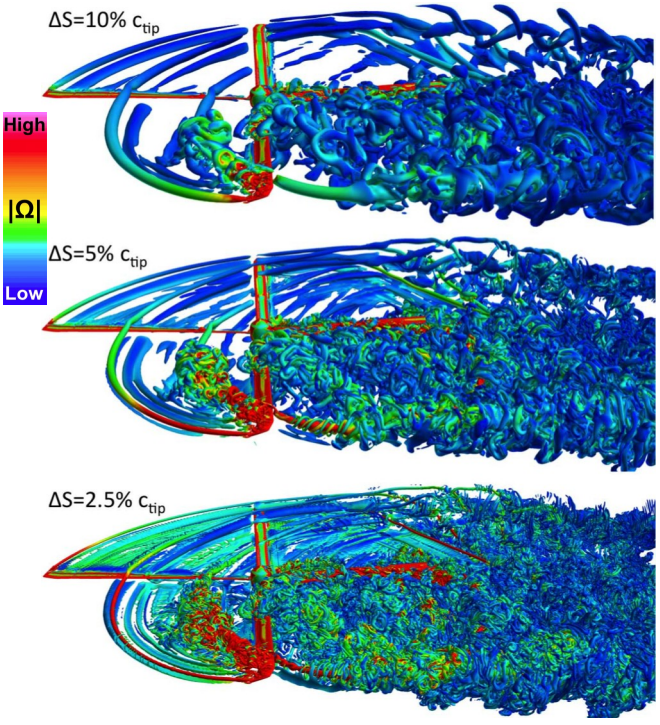

Figure 19. Oblique view of vortex wake colored by vorticity magnitude. Q-criterion iso-surface.

Figure 20 shows the loose coupling convergence history for the pitch, flap, and lag angles and their first harmonics. All three OB grid resolutions are included. All the control angles seem converged in 5 revolutions from impulsive start. The collective and lag angles do have some

small oscillations, unlike the BVI case. This is not surprising since there is significant flow separation on the retreating side, adding a small amount of aperiodicity in the blade loads.

Figure 21 compares the CFD mean airloads with flight-test measurements for all three OB grid resolutions. The normal force is in good agreement with the measurement. However, the normal force peak is under predicted at r/R= 0.775 and 0.865. These locations are in the middle and outer edge of the trim tab. Recall that the actual rotor blade trim tabs each have a custom deflection to ensure similar blade-tip paths during flight and to reduce vibration. The present CFD simulations have zero trim-tab deflections, which could explain this discrepancy. The pitching moment and chord force are also in good agreement. There are three anomalous measurements, i.e., normal and chord force at r/R=0.4, and the pitching moment at r/R =0.865. Once again, all three OB resolutions give virtually identical results.

Figure 22 compares the computed and measured normal force coefficient (mean removed) at four radial locations (see also Fig. 4). The agreement between computation and experiment is good, however, the drop in normal force is under predicted near ψ=90° for the outboard sections. The three grid resolutions are once again in overall good agreement with each other. However, the small differences are larger than in the previous BVI case (C8513). This is particularly true near ψ=0° and 270°. These azimuth angles correspond to significant flow separation. Bousman (Ref. 1) also identified two stall events occurring near these azimuth angles.

The predicted pitching moment coefficient (mean removed) shown in Fig. 23 is in good overall agreement with the flight-test data. The negative pitching moment in the 4th quadrant is best captured with the finest OB grid resolution. However, the difference between the three resolutions is again small, but more pronounced than the previous BVI case. This is especially true near the two dynamic stall events at ψ=0° and 270°.

The chord force coefficient (mean removed) shown in Fig. 24 is also in good overall agreement with the measured data. However, the 4th quadrant CFD oscillation has a greater amplitude than measured at r/R=0.675. The 4th quadrant is particularly challenging due to the strong interaction of the rotor blade with the turbulent wake created by dynamic stall. Moreover, Biedron and Lee-Rausch (Ref. 26) showed that the flight-test measurements of chord force were under resolved, due to a modest number of pressure taps.

Although the accuracy of the airloads prediction for this dynamic stall case had a somewhat greater dependency on the resolution of the vortex-wake grid, compared to the previous BVI case, the overall differences were small from a performance point of view. Moreover, the results reported by Ahmad and Biedron (Ref. 27) for flight counters C8513 and C9017 are very similar to what is reported here. They used the unstructured FUN3D and structured OVERFLOW CFD codes with a ΔS=10% c_{tip} wake grid resolution, similar to the coarsest wake grid resolution presented in this paper.

The coarser grid resolution, ΔS=10%c_{tip}, seems again sufficient for engineering analysis, as in the previous BVI case. It is again assumed that the tip vortex formation is properly resolved through a combination of high-order spatial accuracy and surface-grid resolution, and a DDES approach is used to control the growth of the turbulent wake eddy viscosity to more physically realistic values.

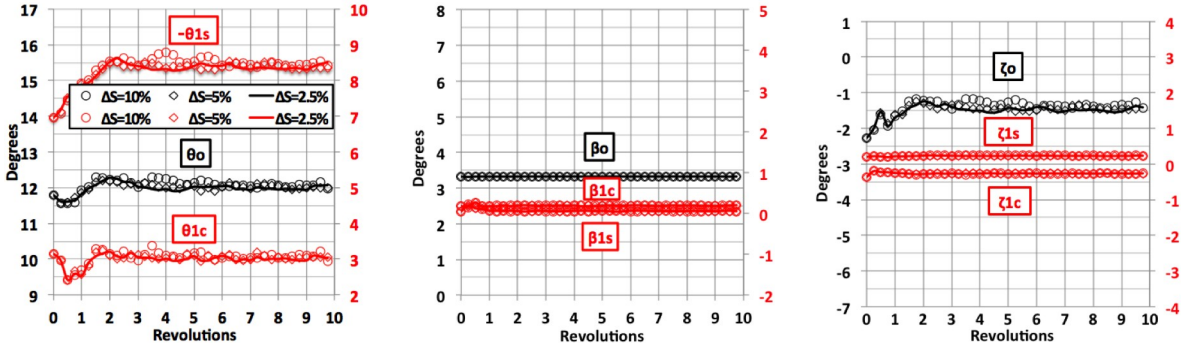

Figure 20. Loose coupling blade-root control angle convergence history.

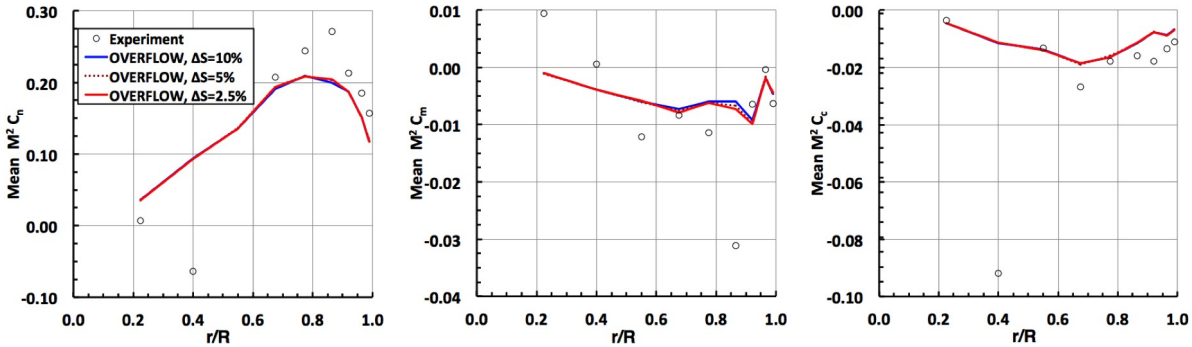

Figure 21. Comparison of mean sectional airloads (azimuthally averaged).

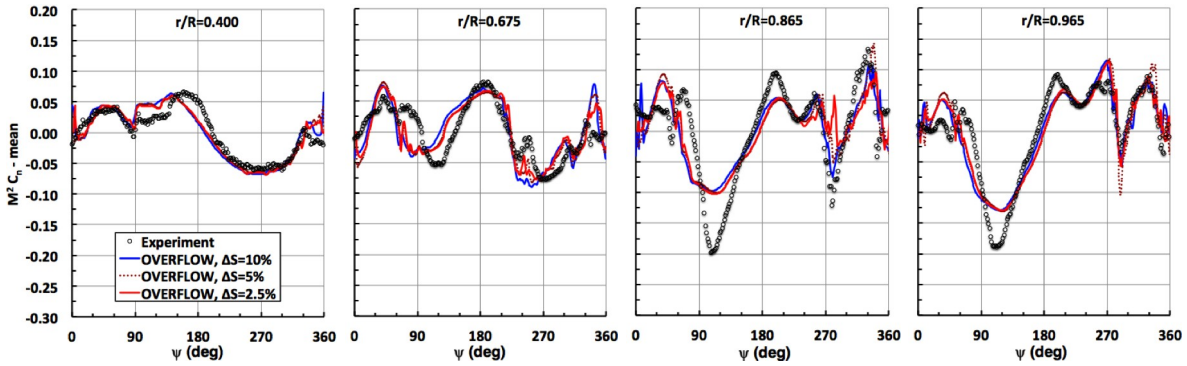

Figure 22 Comparison of normal force coefficient (mean removed) at four radial stations.

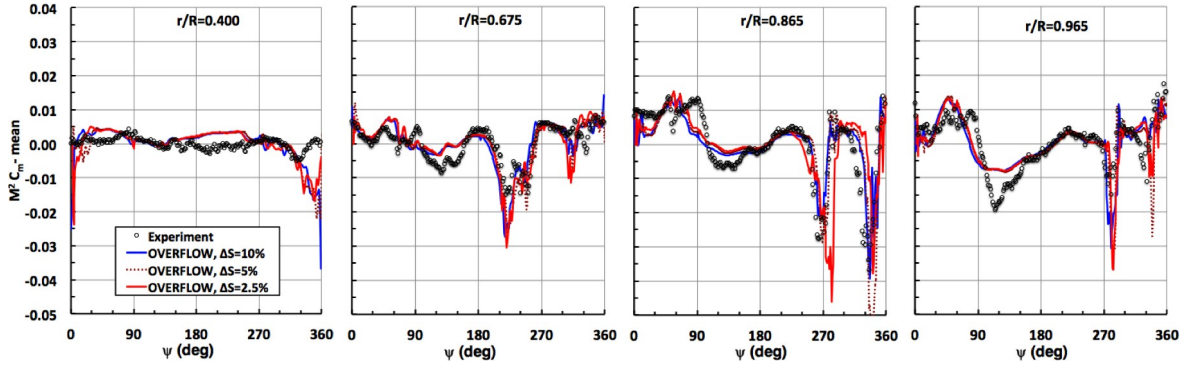

Figure 23. Comparison of pitching moment coefficient (mean removed) at four radial stations.

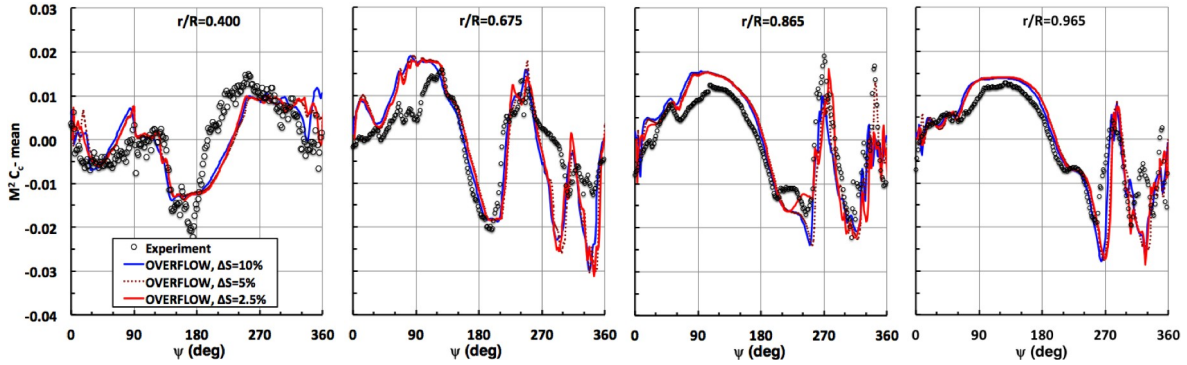

Figure 24. Comparison of chord force coefficient (mean removed) at four radial stations.

Figure 25 shows a close up view of the rotor flowfield in the 3rd and 4th quadrants ($180 \le \psi \le 360°$) on the finest AMR mesh. This image shows there is inboard and outboard flow separation on the rotor blade, and attached flow in the mid-span region of the blade. The outboard separation emits vortex rings that follow alongside the vortex from the previous blade. This illustrates one difference between 2D and 3D dynamic stall. 2D stall involves a leading-edge vortex that lifts off from the airfoil leading edge and advects downwind, past the airfoil trailing edge. Something similar happens in 3D, however, Helmholtz's vortex theorem states that a vortex line can not terminate within a fluid, but on a boundary. Thus when the 3D leading-edge vortex begins to lift off the rotor blade, the vortex line must close in on itself and form a vortex ring. Several vortex rings are emitted as the stall progresses along the blade span during blade rotation.

Figure 25 also shows that the path of the tip vortex is deflected through a combination of BVI and the separated flow. The following blade also has BVI, but the path of the tip vortex is not significantly altered because there is no separated flow on that blade. Thus BVI in combination with dynamic stall may alter the path of a vortex and influence the aeromechanics of the following blades.

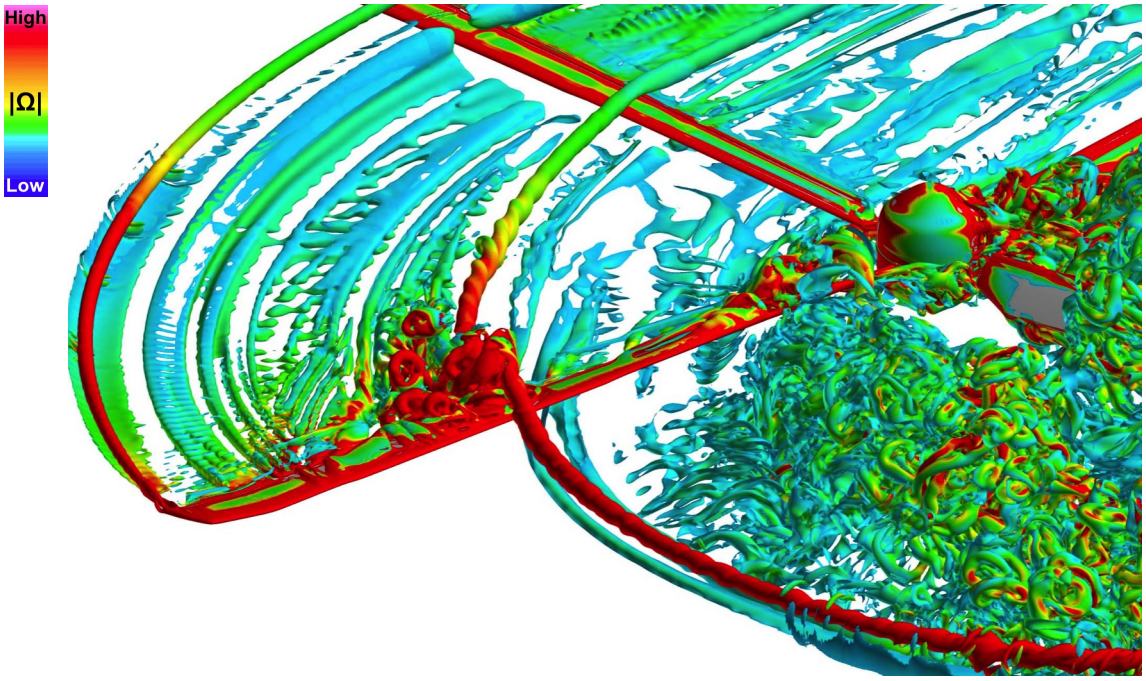

Figure 25. Close-up view of dynamic stall in the 3rd and 4th quadrants. Q-criterion iso-surface.

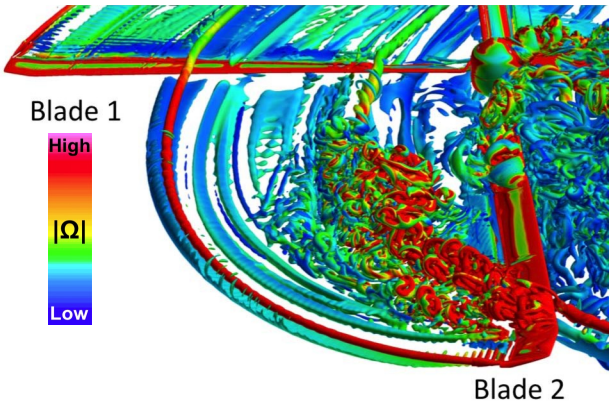

a) Blade 1 at ψ=180°.

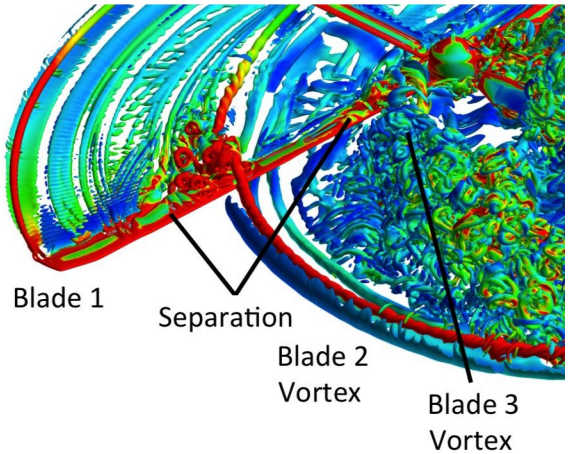

b) Blade 1 at ψ=225°.

Figure 26. Close-up view of vortex induced dynamic stall, ΔS=2.5% c_{tip}. Q-criterion iso-surface.

Figure 26 shows a very strong 3D BVI effect on dynamic stall. The two frames in the figure show Blade 1 at two separate times ($\Delta\psi$=45°). The first frame, Fig. 26a, shows the vortex of Blade 2 passing over Blade 1 with no local flow separation on Blade 1. The second frame, Fig. 26b, shows outboard flow separation on Blade 1, apparently due to the Blade 2 vortex. This vortex has a limiting effect on the inboard progression of stall. Some of the separated flow does manage to work its way underneath the vortex, especially near the blade trailing edge, but the Blade 2 vortex acts like a barrier, restricting inboard flow separation. As Blade 1 continues its rotation, both the Blade 2 vortex and its separation continue to sweep outwards together towards the Blade 1 tip.

The second frame also shows an inboard separation on Blade 1 limited by the vortex from Blade 3, which is two blades upstream in the rotation (see Fig. 6). The Blade 3 vortex and flow separation sweep inboard together along Blade 1, towards the rotor hub. In between these two vortices, there is a region of attached flow.

To sum up, the two vortices from Blades 2 and 3 pass closely over Blade 1 as it retreats away from the freestream. Both vortices appear to trigger inboard and outboard dynamic stall on Blade 1, with attached flow in between the separated regions. A time-dependent animation of the flow shows that the separated flows move along the blade span with the vortices.

Figure 27 shows the local velocity vectors relative to the rotor blade's leading edge, to either side of the outboard vortex (from Blade 2 in Fig. 26b). This vortex reduces the local angle of attack on the inboard side, and increases the local angle of attack on the outboard side. The flow angles on either side of the vortex differ by more than 10 degrees. This tends to promote stall on the outboard side of the vortex, and attached flow on the inboard side of the vortex, as shown in Fig. 26b.

In order to confirm that BVI is the main trigger of dynamic stall for this case, an OVERFLOW simulation was carried out for a UH-60A rotor with only one blade. The same motion and aeroelastic deflections from the 4-bladed coupled simulation were imposed on the single rotor blade.

Figure 28 shows that there is no BVI in the case of a single rotor blade, due to the absence of tip vortices from the other blades. Moreover, there is no outboard flow separation near ψ=270°, confirming the assertion. The inboard separation on the single rotor blade occurs because the blade is retreating away from the freestream (see Fig. 6). A time-dependent flow animation shows that the spanwise extent of this inboard separation is longer than the 4-bladed case, since it lacks the inboard stabilizing effect of BVI.

Figure 29 is taken from Bousman (Ref. 1), and shows his qualitative analysis of the flight-test location of lift stall, moment stall, and regions of separated flow. The locations of the inboard and outboard CFD vortices on Blade 1 are also shown in the figure. Note that the outboard vortex closely follows the experimental location of moment and lift stall. The plot of the outboard vortex position terminates at $\psi \approx 270^{\circ}$ because the CFD vortex drops below the blade at this location. The outboard vortex no longer has a strong influence on the rotor's dynamic stall in the 4th quadrant.

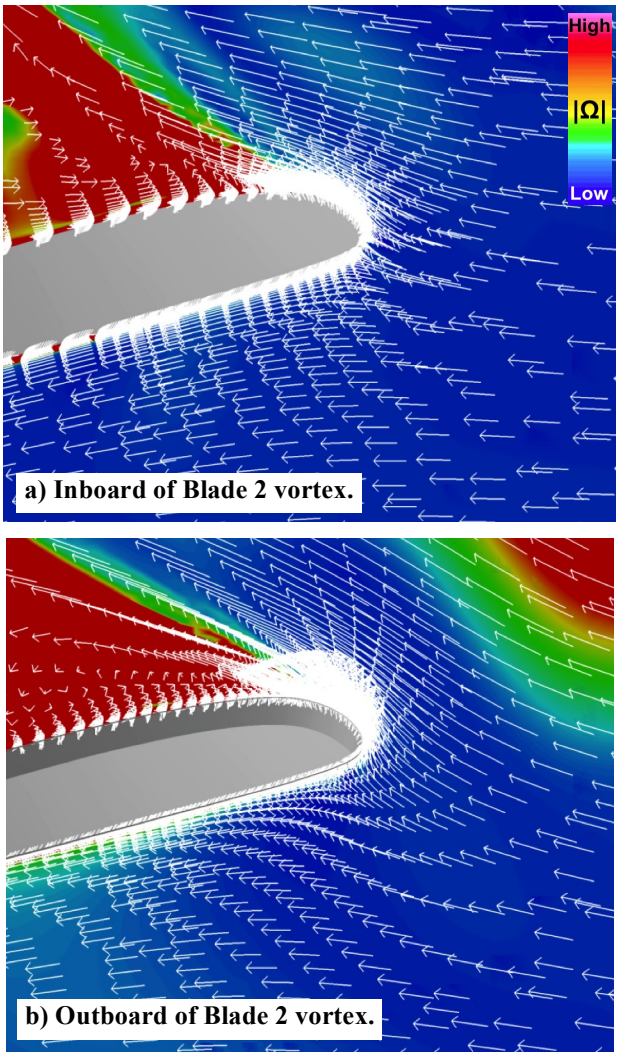

Figure 27. Relative velocity field of Blade 1 induced by the Blade 2 vortex.

Note that Bousman's plot does not indicate any inboard separation, as seen on the CFD simulation. Even without an inboard vortex, there must be inboard flow separation due to reversed flow in this region (see Fig. 6). Bousman (Ref. 9) commented that this inboard separation was not shown because it is difficult to identify flow separation in this region, due to a sparse radial spacing of pressure transducers and very light loading. At the time of his analysis, he felt the inboard region was probably not a key contributor to this dynamic stall flow.

Figure 29 also shows that there were two stall events in the flight-test data, near ψ=270° and 360°. These two stall events also occur in a CFD flow animation (see Fig. 30). The animation in Fig. 30 uses a novel approach of coloring cutting planes with vorticity while rendering lower vorticity values transparent. This allows the view of dynamic stall near the rotor blade surface along the entire blade span.

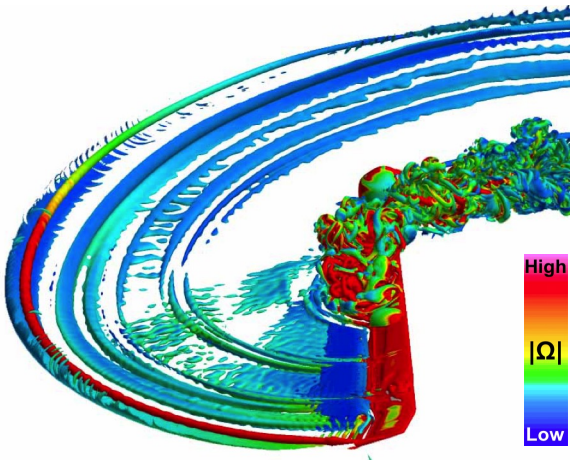

Figure 28. Close-up view of single blade without vortex-induced stall. ψ=270°, ΔS=2.5% c_{tip}. Q-criterion iso-surface.

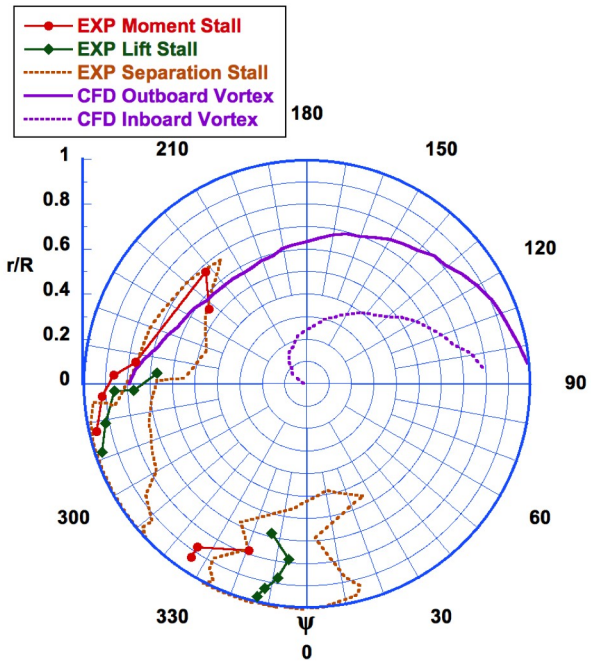

Figure 29. Polar plot of experimental stall locations (Ref. 1) and CFD vortex position. ΔS=2.5% c_{tip}.

Notice that the vertical extent of the first stall event in Fig. 30a is higher than the second stall event in Fig. 30b, similar to the previous 2D dynamic stall example.

To the author's knowledge, this is the first time BVI has been observed to trigger dynamic stall on an actual helicopter rotor. However, BVI induced dynamic stall on a 2D airfoil has been experimentally observed by Zanotti et al. (Ref. 28), and a follow-on CFD analysis (Ref. 29) that provided additional details to the process. In their wind-tunnel experiment, an airfoil spanning the test section underwent and oscillation in angle of attack. Moreover, an upstream vortex generator introduced a vortex perpendicular to the airfoil. They observed that under the right conditions, BVI triggered dynamic stall. They concluded that the induced flowfield from the vortex reduced the angle of attack on one side of the vortex and increased it on the other side, causing dynamic stall. This explanation is similar to the one given in this paper for flight counter C9017.

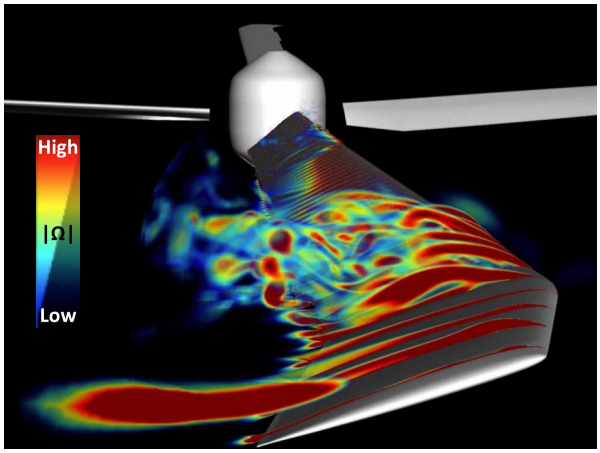

a) First stall event, near ψ=270°.

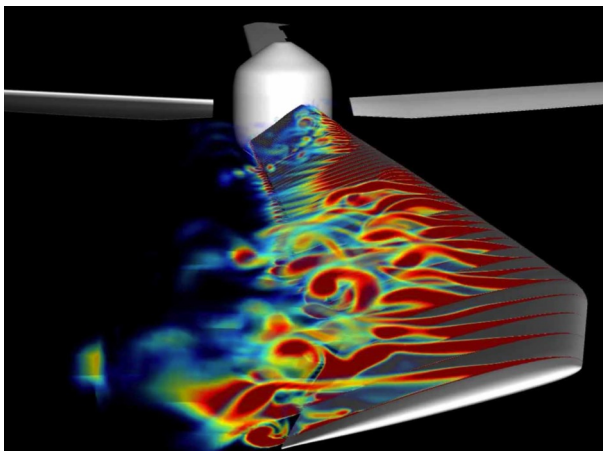

b) Second stall event, near ψ=350°.

Figure 30. View of two dynamic stall events, ΔS=2.5% c_{tip}. Low vorticity values transparent.

Figure 31 shows time-dependent IBFV flow patterns on the upper rotor blade surface (colored by pressure) for ψ=0°, 90°, 180°, and 270°. At ψ=0°, the flow separates near the leading edge along much of the rotor blade. Moreover, separated flow also persists along most of the trailing edge of the rotor blade. This is not surprising considering the blade is immersed in the hub's separated wake (see Figs. 17 and 19), and it is undergoing a second stall event. The flow is mostly attached on the upper blade surface for ψ=90° and 180°, consistent with Fig. 19. Figure 19 also shows two vortices passing over the blade (ψ=180°) near r/R=0.2 and 0.6. The influence of these two vortices on the surface flow can be seen at the same radial locations in Fig. 31. Finally, the upper surface flow at ψ=270° shows inboard and outboard separation, with attached flow in between. This follows from the earlier discussion on how vortices from previous rotor blades can limit the spanwise extent of dynamic stall separation.

Table 5 summarizes the computer wall-clock time used for the three OB AMR resolutions. The computer time and

cost grows significantly with OB grid resolution (see 4th column). The computational efficiency significantly improves with the larger grid sizes (see 6th column). However, the overall cost is about 35% less than the BVI case on the finest mesh (see Table 4) because a smaller L_1 grid is used to surround the rotor blades, allowing the OB AMR to capture more of the vortex wake.

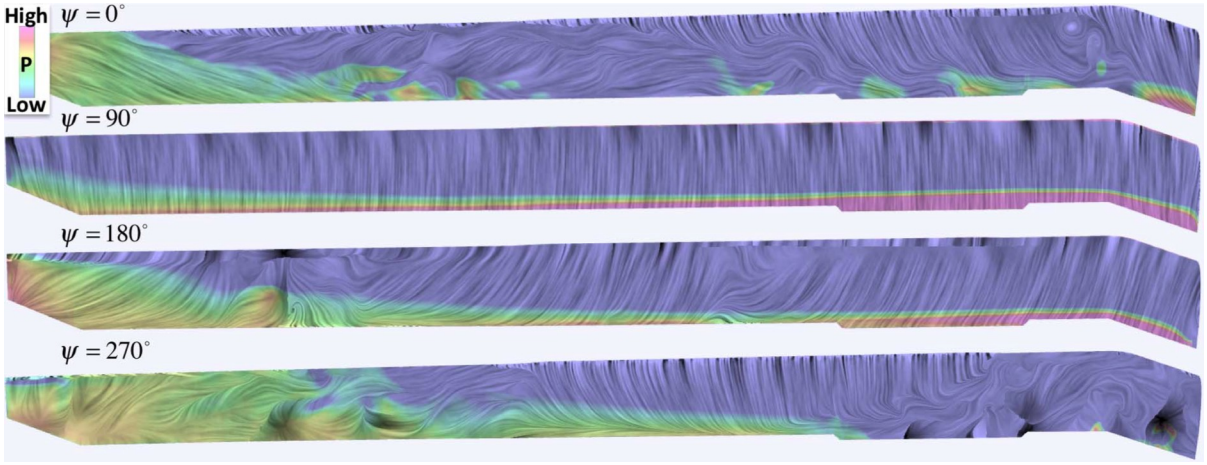

Figure 31. Top view of surface flow colored by pressure. ΔS=2.5% c_{tip}.

Table 5. Summary of computer wall-clock time using 5,628 Broadwell CPU cores with two threads.

Dynamic Stall Counter 9017					
OB AMR Resolution	# Grids	# Grid Points	Time/Rev	Relative Time	Time/Rev/ 100 Million GP
ΔS=10%c_{tip}	868	78 million	5.6 hr	1.0	7.2
ΔS=5%c_{tip}	3,245	236 million	9.5 hr	1.7	4.0
ΔS=2.5%c_{tip}	14,533	1.29 billion	26.0 hr	4.6	2.0

Conclusions

Time-dependent flow simulations for an isolated UH-60A rotor in forward flight have been carried out using the OVERFLOW Navier-Stokes CFD code. Two flow conditions were examined, flight counters C8513 and C9017. These flow conditions correspond to BVI and dynamic stall, respectively. An AMR approach was used to highly resolve the rotor/wake interaction to determine its effect on the predicted airloads. An OVERFLOW simulation for a NACA 0015 airfoil undergoing dynamic stall was also carried out in order to contrast the similarities and differences of 2D and 3D dynamic stall.

- All CFD normal force, pitching moment, and chord force coefficients for the UH-60A compared well with flight-test measurements for both flight counters.
- Wake-grid spacing of ΔS=10%, 5%, and 2.5% c_{tip} had little effect on the predicted normal force, pitching moment, and chord force coefficients. These blade/wake interaction results are similar to previous CFD studies (Refs. 2, 4, and 5) for hover and forward flight, where there wasn't significant blade/wake interaction. Grids ranged in size from 78 million to 1.8 billion grid points.
    - This suggests that a wake grid spacing of ΔS=10% c_{tip} is sufficient for engineering airloads prediction for hover and forward flight. This assumes high-resolution body grids, high-order spatial accuracy, and a hybrid RANS/DDES turbulence model.
- High spatial resolution CFD flow simulations were used together with time-dependent flow visualization to study the complex blade/wake interactions of dynamic stall. There were significant differences between 2D and 3D dynamic stall.
    - 2D dynamic stall can be characterized by a vortex detaching from an airfoil's leading edge and advecting downwind past the trailing edge. However in 3D, Helmholtz's vortex theorem requires that as the leading-edge vortex begins to lift off the rotor blade surface, the vortex line must close in on itself and form a vortex ring. Several vortex rings are emitted as the stall progresses along the blade span.
    - BVI was found to trigger dynamic stall on the UH-60A rotor. The velocity field of a vortex nearly perpendicular to the rotor blade increased the blade's angle of attack on the outboard side of the vortex, causing flow separation on the blade. The vortex also lowered the blade's angle of attack on the

inboard side of the vortex, causing the flow to remain attached on the blade.

- Both inboard and outboard separation regions appeared simultaneously on the upper surface of the UH-60A rotor blade, with attached flow in between. Each region of separated flow was caused by the tip vortex of another blade.
- The phenomenon of BVI triggering dynamic stall has been previously observed in a wind-tunnel experiment (Refs. 28, 29), where an oscillating airfoil was subjected to a vortex perpendicular to its leading edge.
- The successful modeling of three-dimensional dynamic stall with BVI should include an accurate prediction of the vortex trajectories from the other rotor blades.

Acknowledgments

The author would like to thank Mr. Timothy Sandstrom for generating truly state-of-the-art flow visualization, and Mr. Bill Bousman for his helpful discussions of dynamic stall on the UH-60A flight test. This work was funded by NASA's Revolutionary Vertical Lift Technology (RVLT) Project, and utilized the Pleiades supercomputer at NASA's Advanced Supercomputing (NAS) Division.

References

[1]Bousman, W. G., "A Qualitative Examination of Dynamic Stall from Flight Test Data," *Journal of the American Helicopter Society*, Vol. 43, (4), Oct. 1998, pp. 279-295.

[2]Chaderjian, N. M., and Buning, P. G., "High Resolution Navier-Stokes Simulation of Rotor Wakes," Proceedings of the American Helicopter Society 67th Annual Forum, Virginia Beach, VA, May 3-5, 2011.

[3]Egolf , A., Hariharan, N., Narducci, R., and Reed, E., "AIAA Standardized Hover Simulation: Hover Performance Prediction Status and Outstanding Issues," AIAA-2017-1429, January 2017.

[4]Chaderjian, N. M., and Ahmad, J. U., "Detached Eddy Simulation of the UH-60 Rotor Wake Using Adaptive Mesh Refinement," Proceedings of the American Helicopter Society 68th Annual Forum, Fort Worth, TX, May 1-3, 2012.

[5]Chaderjian, N. M., "Advances in Rotor Performance and Turbulent Wake Simulation using DES and Adaptive Mesh Refinement," Paper Number ICCFD7-3506, Presented at the 7th International Conference on Computational Fluid Dynamics (ICCFD7) on the Big Island of Hawaii, July 9-13, 2012.

[6]McAlister, K., and Heineck, J., "Measurements of the Early Development of Trailing Vorticity From a Rotor," NASA/TP-2002-211848, AFDD/TR-02-A001, May 2002.

[7]Bousman, W. G., and Kufeld, R. M., "UH-60A Airloads Catalog," NASA TM 2005-212827, Aug. 2005.

[8]Potsdam, M., Yeo, H., and Johnson, W., "Rotor Airloads Prediction Using Loose Aerodynamic/Structural Coupling," *Journal of Aircraft*, Vol. 43, No. 3, May-June 2006, pp. 732-742.

[9]Bousman, W. G., U.S. Army Aeroflightdynamics Directorate (AMCOM), Moffett Field, CA, Retired. Private conversation, February 2017.

[10]Johnson, W., "Rotorcraft Aerodynamic Models for a Comprehensive Analysis," American Helicopter Society 54th Annual Forum, Washington, D.C., May 1998.

[11]Pulliam, T. H., and Chaussee, D. S., "A Diagonal Form of an Implicit Approximate-Factorization Algorithm," *Journal of Computational Physics*, Vol. 39, No. 2, 1981, pp. 347-363.

[12]Pulliam, T. H., "High Order Accurate Finite-Difference Methods: as seen in OVERFLOW," AIAA-2011-3851, June 2011.

[13]Nichols, R., Tramel, R., and Buning, P., "Solver and Turbulence Model Upgrades to OVERFLOW 2 for Unsteady and High-Speed Flow Applications," AIAA-2006-2824, June 2006.

[14]Nichols, R., and Buning, P., "User's Manual for OVERFLOW 2.1," University of Alabama at Birmingham, Birmingham, AL, 2008.

[15]Buning, P. G., and Pulliam, T. H., "Near-Body Grid Adaption for Overset Grids," AIAA-2016-3326, June 2016.

[16]Buning, P. G., and Pulliam, T. H., "Cartesian Off-Body Grid Adaption for Viscous Time-Accurate Flow Simulations," AIAA-2011-3693, June 2011.

[17]Spalart, P. R., and Allmaras, S. R., "A One-Equation Turbulence Model for Aerodynamic Flows," AIAA-92-0439, January 1992.

[18]Spalart, P., Jou, W-H., Strelets, M., and Allmaras, S. "Comments on the Feasibility of LES for Wings and on a Hybrid RANS/LES Approach," First AFOSR Conference on DNS/LES, August 1997, Greyden Press, Columbus, OH

[19]Shur, M. L., Strelets, M. K., Travin, A. K., and Spalart, P. R., "Turbulence Modeling in Rotating and Curved Channels: Assessing the Spalart-Shur Correction," *AIAA Journal,* Vol. 38, No. 5, May 2000, pp. 784-792.

[20]Spalart, P. R., Deck, S., Sur, M. L., Squires, K. D., Strelets, M., and Travin, A., "A New Version of Detached-Eddy Simulation, Resistant to Ambiguous Grid Densities," *Theoretical and Computational Fluid Dynamics (2006)*, Vol. 20, No. 3, pp. 181-195.

[21]Van Wijk, J. J., "Image Based Flow Visualization," ACM Transactions on Graphics, special issue, Proceedings ACM SIGGRAPH 2002, San Antonio, Texas.

[22]Tan, C. M., and Carr, L. W., "The AFDD International Dynamic Stall Workshop on Correlation of Dynamic Stall Models with 3-D Dynamic Stall data," NASA TM 110375, Jul 1996.

[23]McCroskey, W.J., Carr, L.W., and McAlister, K.W., "Dynamic Stall Experiments on Oscillating Airfoils," *AIAA Journal*, Vol. 14, No. 1, January 1976, pp. 57-63.

[24]Chandrasekhara, M.S., Ahmed, S., "Laser Velocimetry Measurements of Oscillating Airfoil Dynamic Stall Flow Field," AIAA-91-1799, June 1991.

[25]Ramasamy, M., Wilson, J. S., McCroskey, W. J., and Martin, P. B., "Measured Characteristics of Cycle-To-Cycle Variations in Dynamic Stall," Proceedings of the American

Helicopter Society Technical Meeting on Aeromechanics Design for Vertical Lift, San Francisco, CA, January 20-22, 2016.

[26]Biedron, R.T., and Lee-Rausch, E.M., "An Examination of Unsteady Airloads on a UH-60A Rotor: Computation versus Measurement," Proceedings of the American Helicopter Society 68th Annual Forum, Fort Worth, TX, May 1-3, 2012.

[27]Ahmad, J.U., and Biedron, R.T., "Code-to-Code Comparison of CFD/CSD Simulation for a Helicopter Rotor in Forward Flight," AIAA 2011-3819, June 2011.

[28]Zanotti, A., Gibertini, G., and Mencarelli, A., "Experimental Investigation of Perpendicular Vortex Interaction over an Oscillating Airfoil in Dynamic Stall Conditions," Proceedings of the 38th European Rotorcraft Forum, Moscow, Russia, September 3-6, 2013.

[29]Droandi, G., Gibertini, G., Zagaglia, D. and Zanotti, A., "Numerical Investigation of Perpendicular Blade-Vortex-Interaction on a Pitching Airfoil in Light Dynamic Stall," Proceedings of the 72nd American Helicopter Society Annual Forum, West Palm Beach, FL, May 17-19, 2016.